공학석사 학위논문

Laplace-Fourier domain Elastic Full Waveform Inversion using Time domain modeling

시간 영역 파동 전파 모델링을 이용한 라플라스-푸리에 영역 탄성파 완전 파형 역산

2014 년 2 월

서울대학교 대학원

에너지시스템공학부

전 형 구

Laplace-Fourier domain Elastic Full Waveform Inversion using Time domain modeling

시간 영역 파동 전파 모델링을 이용한 라플라스-푸리에 영역 탄성파 완전 파형 역산

지도 교수 신 창 수

이 논문을 공학석사 학위논문으로 제출함
2013년 12 월

서울대학교 대학원
에너지시스템공학부
전 형 구

전형구의 공학석사 학위논문을 인준함
2014 년 1 월

위 원 장 _____ **(인)**

부위원장 _____ **(인)**

위 원 _____ **(인)**

Abstract

To obtain subsurface information from onshore seismic exploration data using full waveform inversion (FWI) based on the acoustic wave equation, elastic waves, such as ground rolls and mode-converted waves, should be suppressed through heavy preprocessing. However, the preprocessing deforms not only the elastic waves but also the acoustic waves. Moreover, it is not easy to separate body waves and surface waves in seismic traces. For these reasons, in the modeling step, we need to generate both types of waves to obtain more similar seismic waves to the real seismic waves. Therefore, elastic full waveform inversion using elastic wave equation is necessary for more accurate full waveform inversion. In addition, elastic full waveform inversion can give better geological information than acoustic full waveform inversion because it inverts P-wave velocity, S-wave velocity and density. Laplace-Fourier domain FWI using time-domain modeling combines time-domain wave propagation modeling and Laplace-Fourier-domain FWI. To obtain forward wavefield and adjoint wavefield in the time domain, we implemented staggered grid finite difference method. The residuals between the recorded and modeled data, virtual sources, hessian matrices and gradient directions were calculated in the Laplace-Fourier domain. We used time domain wave propagation modeling for the forward and adjoint wavefield because it is more intuitive to treat the wavefield in the time domain than in the Laplace-Fourier domain. Moreover, time domain wave propagation modeling using staggered grid finite difference method does not need matrix solver which is necessary for the conventional Laplace-Fourier domain FWI. The optimization procedure is conducted in the Laplace-Fourier domain because

Laplace-Fourier-domain FWI can be applied to real seismic data, which lacks low-frequency components. To validate our proposed algorithm, we performed numerical tests with synthetic data and real exploration data. We applied the algorithm to Model 94 synthetic onshore data and Benjamin Creek real onshore data.

Keywords : Laplace-Fourier domain full waveform inversion, Elastic full waveform inversion, Foothills, onshore data

Student Number : 2012-21009

Contents

List of Figures

List of Tables

Chapter 1 Introduction

The purpose of seismic exploration is to determine the subsurface structure. Several types of migration algorithms, such as Kirchhoff migration and reverse time migration (RTM)(Claerbout, 1971; Whitmore, 1983), have been used to explore the subsurface structures. Migration algorithms require prior knowledge of the subsurface material properties such as velocity or density, and the accuracy of the velocity or density model is the most important factor in obtaining the correct migration image. Moreover, the propertied of subsurface materials are also meaningful because they can give important information which is essential for the petroleum exploration. Many geophysicists have used travel time tomography and FWI to accurately model the properties of subsurface media. Since the development of the adjoint method by Lailly (1983) and Tarantola (1984), FWI has been performed in the time(Mora, 1987; Bunks et al., 1995) and frequency domains (Pratt et al., 1998; Operto et al., 2004).

Even though the development of adjoint method suggested the possibility of FWI algorithm, the practical usage of the FWI still has some difficulties. The first problem is caused by the huge computational cost. To calculate the forward and adjoint wavefield for each shot, we need to solve the impedance matrix related to the model parameters. For the two dimensional case, high efficient computational approach such as direct solver (Kim and kim, 1999; Davis, 2006) or iterative solver (Trefethen and Bau, 1997) are implemented to solve the matrix. However, the extension to three dimensional FWI is challenging because it needs much larger computational resources. Since direct solver requires storing LU factors in random access memory (RAM) or

disk space, iterative solver is widely used to solve the three dimensional problem (Operto et al., 2007). Plessix (2009) used iterative solver with a multigrid preconditioner to perform three dimensional frequency domain FWI. He successfully inverted P-wave velocity from the three dimensional real deepwater OBS data set. Pyun et al. (2011) applied iterative solver to the three dimensional Laplace domain acoutic FWI. Ben-Hadj-Ali et al. (2008) performed acoustic FWI in frequency domain by solving the forward problem with a frequency domain finite difference method based on a massively parallel direct solver. Sirgue et al. (2008) suggested an alternative approach. To obtain frequency domain wavefield, time domain wavefield is calculated from three dimensional time domain finite difference method and the wavefield is transformed to the frequency domain through the discrete fourier transform. Kim et al. (2013) used the same approach and applied it to the three dimensional Laplace-Fourier domain acoustic FWI. In this research we also followed Sirgue et al. (2008)'s approach and applied it to the two dimensional Laplace-Fourier domain elastic FWI.

The second problem is generated from the nonlinearity of the inverse problem. FWI is considered as nonlinear problem because of the existence of local minimum points in the objective function. Especially, when the starting model is located far from the real model, the problem of nonlinearity becomes severer (Gauthier et al., 1986). To overcome this problem, Bunks et al. (1995) suggested the multiscale approach to the seismic inversion problem and reduced the local minima by using the multigrid method. Shipp and Singh (2002) and Sirgue and Pratt (2004) selected the starting model which is similar to the real model to avoid the problem of local minimum. There are a few approach to reduce the local minima in objective function by suggesting the robust objective function. Guitton and Symes (2003) applied Huber norm

(Huber, 1973) to the noisy seismic data inversion. Shin and Min (2006) proposed logarithmic objective function. By taking the logarithmic objective function, the wavefield can be separated into amplitude and phase, and objective function can be constructed from amplitude only, phase only and both. Shin and Cha (2008) suggested Laplace domain FWI using logarithmic objective function and large damping constants. The Laplace domain FWI cannot invert the high resolution image, but can attenuate the nonlinearity in FWI and give a long wavelength result even when the seismic data is lack of low-frequency components. For the onshore data, the problem of nonlinearity is severer than onshore data. For the onshore seismic data, the seismic waves are recorded in receivers after being filtered by water which is acoustic media. However, for the onshore data, the energy generated from the source makes not only body waves but also surface waves which contain the large energy. The co-existence of body waves and surface waves increases the nonlinearity of the onshore data FWI. For the application of the FWI, there were some attempts to mute or attenuate the surface waves to separate them from the body waves. Sheng et al. (2006) used early arrival waveform tomography with time window which can exclude the surface waves or other unpredicted waves. Operto et al. (2004) and Ravaut et al. (2004) performed several preprocessing steps to improve signal to noise ratio and transformed the data suitable for the acoustic full waveform tomography through the acoustic approximation. Brenders and Pratt (2007) removed phases in the data which cannot be modeled by the acoustic wave equation such as shear wave and mode converted wave for the stable convergence in frequency domain FWI. Also the rayleigh waves which is dominant near the surface was suppressed by offset-dependent cosine taper. Ha et al. (2010) used acoustic FWI to invert the P-wave velocity of synthetic onshore and offshore seismic data in the

Laplace domain with minimum preprocessing. The Laplace domain acoustic FWI yielded correct long wavelength velocity model even with the noise originated from elastic waves.

Although preprocessing can suppress the surface waves or unwanted noises, it also alters important signals and degrades the imaging result because P-waves are typically mixed with the other signals (Yan and Sava, 2008). To minimize the damage on the recorded signals, elastic FWI should be used. The studies to invert the elastic components of subsurface material have been performed in both global scale and local scale.

Tarantola (1986) proposed a strategy for nonlinear inversion of real seismic reflection data. He solved inverse problem with sequential optimization technique. First, P-wave velocity and impedance are optimized. Then, optimizing for the S-wave velocity and impedance is performed. Finally density is optimized. Mora (1987) performed an inversion using P-wave velocity, S-wave velocity and density rather than using Lame constants. He validate his approach using multioffset seismic data generated from synthetic model and showed the excellent spatial resolution of the high-frequency components of elastic parameters. Crase et al. (1990) inverted P-impedance and S-impedance from real marine reflection data by using several criteria. Tests showed the Cauchy and hyperbolic secant criteria give good results in both noise-free and noise-added data. Igel et al. (1996) inverted P-impedance and Poisson's ratio. He suggested two step approach; the first step is inverting P-impedance and the second step is inverting Poisson's ratio with inverted P-impedance. Poisson's ratio only makes sense when the P-impedance model is given with high accuracy. Sears et al. (2008) exploited both P-wave and mode-converted S-waves from wide-angle, multicomponent OBC data set to invert both P-wave and S-wave velocity by using time domain FWI algorithm.

They tested FWI with different component-types and temporal windowing. Fichtner et al. (2009, 2013) performed full waveform tomography and full waveform inversion in the global scale. Through these studies, they resolved the details of crustal and mantle structure. Choi et al. (2008) implemented frequency domain FWI to invert P-wave velocity, S-wave velocity and density in acoustic-elastic coupled media. He applied the algorithm to the synthetic data and real offshore data using linear increase with depth model as initial model. Bae et al. (2010) performed Laplace domain FWI in acoustic-elastic coupled media to obtain long wavelength P-wave velocity and S-wave velocity results. Both studies are based on the finite-element modelling technique and used acoustic wave equation for the acoustic media and elastic wave equation for the elastic media. To combine the acoustic wave equation and elastic wave equation, they used continuity condition for interface. Brossier et al. (2009) proposed frequency domain elastic FWI for onshore synthetic data by using complex frequencies which is equivalent to damped seismograms in the time domain and offset-dependent weighting function. They showed successive inversion of overlapping frequency groups outperforms successive inversion of single frequencies. Romdhane et al. (2011) showed frequency domain elastic FWI is effective to image heterogeneous shallow structures when the data contains both surface waves and body waves. Two strategies were taken to attenuate the strong nonlinearity. First, they took successive inversion technique with overlapping frequency groups. The second is to introduce time damping to the seismic signal. The algorithm was applied to a realistic onshore synthetic data and inverted P-wave and S-wave velocity model.

Based on these studies, we inverted the P-wave velocity, the S-wave velocity and density from synthetic and real onshore data using Laplace-Fourier

domain FWI with time domain wave propagation modeling. Conventional Laplace-Fourier domain FWI suggested by Shin and Cha (2009) uses matrix solver for the forward and adjoint wavefield. On the other hand, we followed Sirgue et al. (2008)'s approach and combined time domain wave propagation modeling and the Laplace-Fourier domain FWI.

In this paper, we first briefly review time domain wave propagation modeling using staggered-grid finite-difference method and Laplace-Fourier domain FWI. Second, the Laplace-Fourier domain FWI using time domain modeling algorithm is introduced. Third, we apply our algorithm to Model 94 synthetic onshore data, compare the Laplace-Fourier-transformed wavefields of the recorded and modeled data, plot extracted time traces and perform frequency-domain FWI with a low damping constant (Brossier et al., 2009) to obtain high-resolution images. Finally, we apply Laplace-Fourier domain FWI to Benjamin Creek real onshore data and compare the RTM images obtained using the initial and inverted velocities.

Chapter 2 Theory

2.1 Time domain wave propagation modeling

The wave equation in two dimensional elastic media is defined by Newton's equation of motion:

$$\rho \frac{\partial^2 u_x}{\partial t^2} = \frac{\partial}{\partial x}\left((\lambda + 2\mu)\frac{\partial u_x}{\partial x} + \lambda \frac{\partial u_z}{\partial z}\right) + \frac{\partial}{\partial z}\left(\mu\left(\frac{\partial u_z}{\partial x} + \frac{\partial u_x}{\partial z}\right)\right) + f_x \ , \qquad (1)$$

$$\rho \frac{\partial^2 u_z}{\partial t^2} = \frac{\partial}{\partial x}\left(\mu\left(\frac{\partial u_z}{\partial x} + \frac{\partial u_x}{\partial z}\right)\right) + \frac{\partial}{\partial z}\left((\lambda + 2\mu)\frac{\partial u_z}{\partial z} + \lambda \frac{\partial u_x}{\partial x}\right) + f_z \qquad (2)$$

(u_x, u_z) are the horizontal and vertical displacement components; (f_x, f_z) are the body forces; λ and μ are the Lam*é* coefficients and ρ is density.

Velocity can be expressed as first derivative of displacement respect to time. Therefore, the equation (1) and (2) can be changed into first-order differential equation respect to time by substituting displacement components with velocity components. Then, the equations (1) and (2) are rewritten as follows.

$$\rho \frac{\partial v_X}{\partial t} = \frac{\partial \tau_{xx}}{\partial x} + \frac{\partial \tau_{xz}}{\partial z} + f_x \qquad (3)$$

and

$$\rho \frac{\partial v_z}{\partial t} = \frac{\partial \tau_{xz}}{\partial x} + \frac{\partial \tau_{xx}}{\partial z} + f_z \ . \qquad (4)$$

where,

$$\frac{\partial \tau_{xx}}{\partial t} = (\lambda + 2\mu)\frac{\partial v_x}{\partial x} + \lambda \frac{\partial v_z}{\partial z} \ , \qquad (5)$$

$$\frac{\partial \tau_{zz}}{\partial t} = (\lambda + 2\mu)\frac{\partial v_z}{\partial z} + \lambda \frac{\partial v_x}{\partial x} \tag{6}$$

and

$$\frac{\partial \tau_{xz}}{\partial t} = \mu \left(\frac{\partial v_x}{\partial x} + \frac{\partial z}{\partial z}\right) . \tag{7}$$

$(\mathrm{v_x}, v_z)$ are the velocity components and $(\tau_{\mathrm{xx}}, \tau_{xz}, \tau_{zz})$ are the stress components. We exploited a staggered-grid finite-difference method (Madariaga, 1976; Virieux, 1986; Levander, 1988; Graves, 1996) for the wave propagation modeling in time domain and adapted sponge boundary condition (Cerjan et al., 1985) to reduce the edge reflection. In this study, we obtained forward modeled wavefield and adjoint wavefield in the time domain and transformed them to the Laplace-Fourier domain for the Laplace-Fourier domain FWI.

2.2 Wavefield in the Laplace-Fourier domain

From Shin and Cha (2009), the wavefield in the Laplace-Fourier domain is expressed as

$$\tilde{u}(s) = \int_0^\infty u(t)e^{-st}dt = \int_0^\infty u(t)e^{-\sigma t}e^{-i\omega t}dt \ , \qquad (8)$$

where, complex number s is substituted by $\sigma + i\omega$. σ is a Laplace damping constant, ω is an imaginary part of the complex frequency, $u(t)$ is a time domain wavefield and $\tilde{u}(s)$ is the Laplace-transformed wavefield. Shin and Cha (2008) performed Laplace-domain FWI with the Laplace-transformed wavefield which is the zero frequency component of the Fourier transform of the damped wavefield where σ is real number and ω is zero. If we choose σ as widely varying variables and ω as small variables, it is Laplace-Fourier-domain FWI (Shin and Cha, 2009). If we choose σ as 0 (Pratt et al., 1998; Operto et al., 2004) or small variables (Brossier et al., 2009), and ω as widely varying variables, it is frequency-domain FWI.

2.3 Full waveform inversion in the Laplace-Fourier domain

The logarithmic objective function at an angular frequency can be expressed as

$$\mathrm{E} = \sum_{i=1}^{n_s}\sum_{j=1}^{n_r}(ln\tilde{u}_{ij} - ln\tilde{d}_{ij})\left(ln\tilde{u}_{ij} - ln\tilde{d}_{ij}\right)^{*} \ , \tag{9}$$

where $\mathrm{n_s}$ is the number of shots, $\mathrm{n_r}$ is the number of receivers, * denotes the complex conjugate and $\tilde{u}_{ij}$ and $\tilde{d}_{ij}$ are the modeled and recorded displacement in the Laplace-Fourier domain at the $\mathrm{i^{th}}$ shot and $\mathrm{j^{th}}$ receiver, respectively.

By taking the partial derivative of the objective function with respect to a model parameter $\mathrm{m_l}$, we can obtain a gradient vector as follows:

$$\frac{\partial E}{\partial m_l} = \sum_{i=1}^{n_s} Re\left[\left(\frac{\partial \tilde{\boldsymbol{u}}_i}{\partial \tilde{m}_l}\right)^T \boldsymbol{r}_i^*\right] = Re[\boldsymbol{J}^T \boldsymbol{r}_i^*] \tag{10}$$

where,

$$\tilde{\boldsymbol{u}}_i = [\tilde{u}_{i1}\ \tilde{u}_{i2}\ \tilde{u}_{i3}\ \cdots\ \tilde{u}_{in}]^T \ , \tag{11}$$

$$\mathbf{r}_\mathrm{i}^* = \left[\frac{1}{\tilde{u}_{i1}} ln\left(\frac{\tilde{u}_{i1}}{\tilde{d}_{i1}}\right)^{*}\ \ \frac{1}{\tilde{u}_{i2}} ln\left(\frac{\tilde{u}_{i2}}{\tilde{d}_{i2}}\right)^{*}\ \ \cdots\ \ \frac{1}{\tilde{u}_{in_r}} ln\left(\frac{\tilde{u}_{in_r}}{\tilde{d}_{in_r}}\right)^{*}\ \ 0\ \ \cdots\ \ 0\right]^T \tag{12}$$

and

$$\mathbf{J} = \frac{\partial \tilde{\mathbf{u}}_i}{\partial \tilde{m}_l} \ . \tag{13}$$

Re means the real part of a complex value, n is the number of nodes in domain, $\mathbf{r}_\mathrm{i}$ is a residual vector, $\mathbf{J}$ is the Frech*é*t derivative matrix and T is a

transposed matrix.

The wave equation in the Laplace-Fourier domain can be expressed as

$$\mathbf{S}\tilde{\boldsymbol{u}} = \boldsymbol{f} \tag{14}$$

with

$$\mathbf{S} = \mathbf{M}s^2 + \boldsymbol{K} \tag{15}$$

S is an impedance matrix, **u** is a vector for the modeled wavefields , **f** is a source vector, **M** is a mass matrix, **K** is a stiffness matrix and s is a complex frequency. By taking the partial derivative of equation (14) with respect to model parameter m_l, the partial derivative wavefields can be obtained as follows:

$$\frac{\partial \tilde{\boldsymbol{u}}}{\partial m_l} = \boldsymbol{S}^{-1}\left(-\frac{\partial \boldsymbol{S}}{\partial m_l}\tilde{\boldsymbol{u}}\right) = \boldsymbol{S}^{-1}\boldsymbol{v}_l \tag{16}$$

where,

$$\boldsymbol{v}_l = -\frac{\partial \boldsymbol{S}}{\partial m_l}\tilde{\boldsymbol{u}} \ . \tag{17}$$

$\boldsymbol{v}_l$ is a virtual-source vector for l^{th} model parameter. By putting equation (16) into equation (10), the gradient vector can be expressed by using the impedance matrix.

$$\frac{\partial E}{\partial m_l} = \sum_{i=1}^{n_s} Re[(\boldsymbol{S}^{-1}\boldsymbol{v}_l)^T \boldsymbol{r}_i^*] = \sum_{i=1}^{n_s} Re\left[\boldsymbol{v}_l^T \boldsymbol{S}^{-1}\boldsymbol{r}_i^*\right] \tag{18}$$

where, $\mathbf{S}^{-1}\boldsymbol{r}_i^*$ is the adjoint wavefield in the Laplace-Fourier domain.

For the adjoint wavefield, we need to obtain it in the time domain and transform it to the Laplace-Fourier domain because we exploit Laplace-domain FWI using time domain modeling algorithm. The adjoint wavefield can be obtained in the time domain by using time domain wave propagation

modeling with the equation through (3) to (7). We perform forward modeling by giving the vertical source in source term f_z in the equation (4). In the same context, to calculate adjoint wavefield in the time domain, we need to perform time domain wave propagation modeling with the equation through (3) to (7) by using the residual vector $\mathbf{r}_i^*$ in equation (12) as a vertical source in the equation (4).

2.4 The construction of the virtual source vectors

In this study, we calculate virtual source vector in the Laplace-Fourier domain with the wavefield transformed from the time domain by the equation 8. Using the finite element formulation, the impedance matrix in the Laplace-Fourier domain is expressed in equation (15) and virtual source that we have to calculate is expressed in equation (17). The mass matrix for an element in two-dimensional domain $\mathrm{u}(\mathrm{x},\mathrm{z})$ can be calculated by using the first-order basis function ϕ.

$$\mathbf{M}_{\mathrm{e}} = \int_{\Omega} \boldsymbol{N}^{T}\boldsymbol{P}\boldsymbol{N}\, d\Omega \tag{19}$$

where

$$\boldsymbol{N} = \begin{pmatrix} \phi_1 & 0 & \phi_2 & 0 & \phi_3 & 0 & \phi_4 & 0 \\ 0 & \phi_1 & 0 & \phi_2 & 0 & \phi_3 & 0 & \phi_4 \end{pmatrix} \tag{20}$$

and

$$\mathrm{P} = \begin{pmatrix} \rho & 0 \\ 0 & \rho \end{pmatrix} \quad . \tag{21}$$

In the same manner, the stiffness matrix for an element Ω in $\mathbf{u}(\mathrm{x},\mathrm{z})$ can be calculated by using the first-order basis function ϕ.

$$\mathbf{K}_{e} = \int_{\Omega} \boldsymbol{B}^{T}\boldsymbol{C}\boldsymbol{B}\, d\Omega \tag{22}$$

where

$$\boldsymbol{B} = \begin{bmatrix} \frac{\partial \phi_1}{\partial x} & 0 & \frac{\partial \phi_2}{\partial x} & 0 & \frac{\partial \phi_3}{\partial x} & 0 & \frac{\partial \phi_4}{\partial x} & 0 \\ 0 & \frac{\partial \phi_1}{\partial z} & 0 & \frac{\partial \phi_2}{\partial z} & 0 & \frac{\partial \phi_3}{\partial z} & 0 & \frac{\partial \phi_4}{\partial z} \\ \frac{\partial \phi_1}{\partial z} & \frac{\partial \phi_1}{\partial x} & \frac{\partial \phi_2}{\partial z} & \frac{\partial \phi_2}{\partial x} & \frac{\partial \phi_3}{\partial z} & \frac{\partial \phi_3}{\partial x} & \frac{\partial \phi_4}{\partial z} & \frac{\partial 4}{\partial x} \end{bmatrix} \tag{23}$$

and

$$\mathbf{C} = \begin{bmatrix} \rho v_p^2 & \rho v_p^2 & 0 \\ \rho v_p^2 - 2\rho v_s^2 & \rho v_p^2 & 0 \\ 0 & 0 & \rho v_s^2 \end{bmatrix} \tag{24}$$

where ρ is the density and v_p and v_s are the P-wave and S-wave velocities, respectively. Therefore, the virtual-source vectors for constructing the partial-derivative wavefields with respect to the P-wave and S-wave velocities and the density can be obtained for an element as follows:

$$-\frac{\partial \boldsymbol{S}}{\partial v_p}\boldsymbol{u} = -\frac{\partial \boldsymbol{K}_e}{\partial v_p}\boldsymbol{u} = -\int_\Omega \boldsymbol{B}^T \begin{bmatrix} 2\rho v_p & 2\rho v_p & 0 \\ 2\rho v_p & 2\rho v_p & 0 \\ 0 & 0 & 0 \end{bmatrix} \boldsymbol{B}\, d\Omega \boldsymbol{u} \tag{25}$$

and

$$-\frac{\partial \boldsymbol{S}}{\partial v_s}\boldsymbol{u} = -\frac{\partial \boldsymbol{K}_e}{\partial v_s}\boldsymbol{u} = -\int_\Omega \boldsymbol{B}^T \begin{bmatrix} 0 & -4\rho v_s & 0 \\ -4\rho v_s & 0 & 0 \\ 0 & 0 & 2\rho v_s \end{bmatrix} \boldsymbol{B}\, d\Omega \boldsymbol{u}\ . \tag{26}$$

The virtual-source vector for the density can be expressed as follows:

$$-\frac{\partial \boldsymbol{S}}{\partial \rho}\boldsymbol{u} = -s^2 \frac{\partial \boldsymbol{M}_e}{\partial \rho}\boldsymbol{u} = -s^2 \int_\Omega \boldsymbol{N}^T \begin{bmatrix} 1 & 0 \\ 0 & 1 \end{bmatrix} \boldsymbol{N}\, d\Omega \boldsymbol{u}\ . \tag{27}$$

2.5 Update model parameters with the pseudo-Hessian

From Pratt et al. (1998) hessian matrix can be expressed as follows:

$$\mathbf{H} = \mathbf{H}_{\mathrm{a}} + \boldsymbol{R} \tag{28}$$

where,

$$\mathbf{H}_{\mathrm{a}} = Re(\boldsymbol{J}^T\boldsymbol{J}^*) \tag{29}$$

and

$$\mathbf{R} = \mathrm{Re}\left\{\left[\left(\frac{\partial}{\partial m_1}\boldsymbol{J}^T\right)\boldsymbol{r}^* \;\; \left(\frac{\partial}{\partial m_2}\boldsymbol{J}^T\right)\boldsymbol{r}^* \;\; \cdots \;\; \left(\frac{\partial}{\partial m_n}\boldsymbol{J}^T\right)\boldsymbol{r}^* \;\; \right]\right\} \tag{30}$$

$\mathbf{H}_{\mathrm{a}}$ is the approximate Hessian matrix. With approximate Hessian matrix, we obtain the Gauss-Newton formula

$$\mathrm{m}_{\mathrm{l}}^{k+1} = m_l^k - \boldsymbol{H}_a^{-1}\nabla_{\mathrm{m}}E \tag{31}$$

where, $\mathrm{m}_{\mathrm{l}}^{\mathrm{k}}$ is the l^{th} model parameter at the k^{th} iteration and $\nabla_{\mathrm{m}}E$ is the gradient direction. However, full Hessian matrix $\mathbf{H}$ and approximate Hessian matrix $\mathbf{H}_{\mathrm{a}}$need a lot of computational cost. To reduce the computational cost, Shin et al. (2001) normalized the gradient direction with the pseudo-Hessian using the diagonal elements of the Hessian matrix for the stable convergence of the FWI. The pseudo-Hessian matrix is given by

$$\mathbf{H}_{\mathrm{p}} = Re(\boldsymbol{v}_l^T\boldsymbol{v}_l^*) \tag{32}$$

Ha et al. (2009) updated the model parameter with the normalized gradient. Chung et al. (2010) also used normalized gradient to invert P-wave velocity, S-wave velocity and density in the Laplace domain. In this study, we followed

Chung et al. (2010)'s approach and the gradient direction for a single complex frequency is as follows:

$$m_l^{k+1} = m_l^k - \alpha \times NRM\left[\frac{\sum_{i=1}^{n_s} Re(\boldsymbol{v}_l^T \boldsymbol{S}^{-1} \boldsymbol{r}_i^*)}{\sum_{i=1}^{n_s} Re(\boldsymbol{v}_l^T \boldsymbol{v}_l^*) + \lambda I}\right] \quad (33)$$

where, m_l^k is the l^{th} model parameter at the k^{th} iteration, i is the shot index, n_s is the number of shots, α is the step length, λ represents the stabilizing constant (Marquardt, 1963) and NRM is the normalization operator.

2.6 Algorithm of the Laplace-Fourier domain FWI using time domain modeling

In the Laplace-Fourier domain FWI using time domain wave propagation modeling, forward and adjoint wavefield modeling are conducted in the time domain. The residual, virtual source, pseudo-hessian and gradient direction are calculated in the Laplace-Fourier domain. The specific procedure is illustrated in Figure 1. We first need to perform wave propagation modeling in the time domain. Then, the Laplace-Fourier transform of the recorded and modeled data is executed. Next, the residuals between the recorded and modeled data are calculated in the Laplace-Fourier domain. Then, the inverse Laplace-Fourier transform must be performed to calculate the adjoint wavefield. The virtual source is obtained from the residual vector, and the hessian is computed from the virtual source. The gradient direction is then calculated from the adjoint wavefield and virtual source. Finally, the model parameters are updated with the gradient direction and hessian.

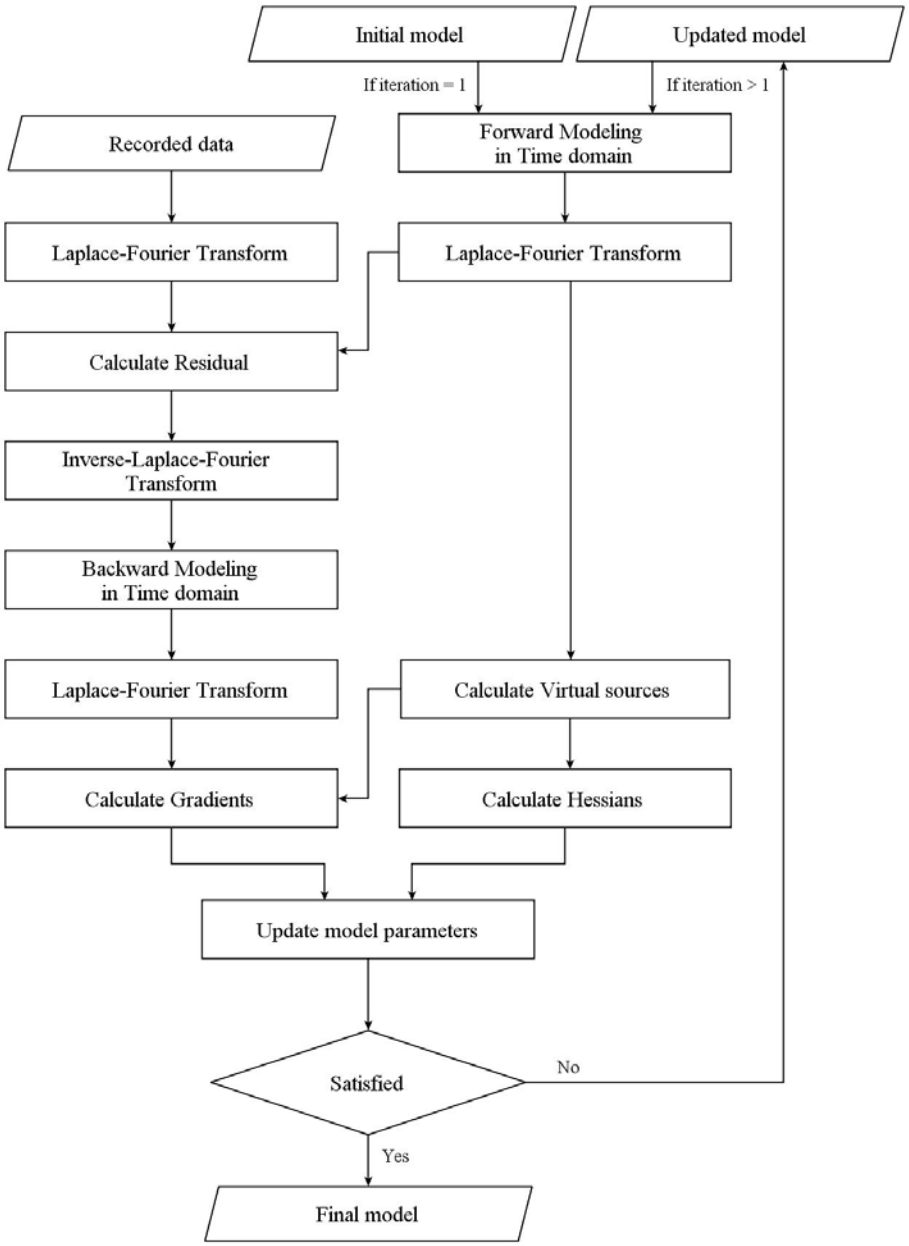

Figure 1. Algorithm of the Laplace-Fourier domain FWI using time domain modeling

Chapter 3 Numerical Examples

3.1 Comparison of the memory and time

For the conventional Laplace-Fourier domain FWI, matrix related to model parameters should be solved by matrix solver. When two dimensional FWI is performed, direct matrix solver and iterative matrix solver are widely used because using them is efficient to solve the matrix and makes easy to parallelize the algorithm. However, when the domain becomes larger, the more memory space is necessary. For this reason, Sirgue et al. (2008) and Kim et al. (2013) suggested alternative approach which uses time domain wave propagation modeling. When the forward and adjoint wavefields are computed in the time domain, there is no memory problem because time domain wave propagation algorithm usually needs a little size of memory. In this section, we compared the requirement of memory and time to perform the wave propagation modeling used in conventional Laplace-Fourier domain FWI algorithm and suggested Laplace-Fourier domain FWI algorithm. For the conventional Laplace-Fourier domain FWI, finite element method (FEM) was implemented with matrix solver and the modeling was performed in the Laplace-Fourier domain. The suggested FWI algorithm used staggered-grid finite-difference method (FDM) for the time domain wave propagation modeling without matrix solver and transformed the wavefield to the Laplace-Fourier domain to perform Laplace-Fourier domain FWI. The parameters used for the test are in Table 1. Test was performed for the mono-frequency and single shot data with single CPU core, because these parameters are the

ground value for the parallel computation with muti-CPUs. 10 tests were conducted with various domain size from 101×101 to 1001×1001. Intel® Xeon® E5420 CPU with 32Gb of maximum memory was used for the test. For the memory test, the highest memory usage was checked while performing wave propagation modeling by using “gnome-system-monitor” program. For the computing time test, Fortran90 built-in function “cpu_time” was implemented. Domain-wise Multi-frontal Solver (DMS) suggested by Kim and Kim (1999) was used as direct matrix solver. Test results are shown in Table 2 and Figure 2. Required (a) memory and (b) time to perform wave propagation modeling in the time domain using FDM and the Laplace-Fourier domain using FEM.Figure 2. Required memory to solve the matrix is larger than memory to perform the time domain modeling. Required time shows same aspect as the memory requirement. It means that use of time domain modeling without matrix solver is more efficient than using Laplace-Fourier domain modeling with matrix solver. When there are many shot gathers to be generated, using matrix solver has an advantage in the computing time because it needs only one matrix factorization procedure per a frequency, which takes most of the time. Even in that case, using time domain modeling still has an advantage in the memory requirement. For the parallel computation with multi-CPUs, shots are parallelized for the Laplace-Fourier domain FWI using time domain modeling and frequencies are parallelized for the conventional Laplace-Fourier domain FWI.

Parameter	dx (m)	dz (m)	dt (s)	nt	Domain (x,z)
Value	25	25	0.002	2000	n×(101,101), (n=1,2,⋯,10)

Table 1. Parameters used for the comparison test of memory and time

		FDM		FEM	
	Domain size	Memory (Mb)	Time (s)	Memory (Mb)	Time (s)
1	101x101	1	0.458	49.3	1.076
2	201x201	3	1.847	283	4.129
3	301x301	7	3.685	620	9.88
4	401x401	10	6.61	1100	19.036
5	501x501	16	11.824	1700	31.68
6	601x601	21	17.751	2400	50.974
7	701x701	28	23.889	3500	82.478
8	801x801	35	30.695	4700	108.889
9	901x901	44	37.813	5500	147.799
10	1001x1001	53	48.812	6900	185.564

Table 2. Required memory and time to perform wave propagation modeling in the time domain using FDM and the Laplace-Fourier domain using FEM.

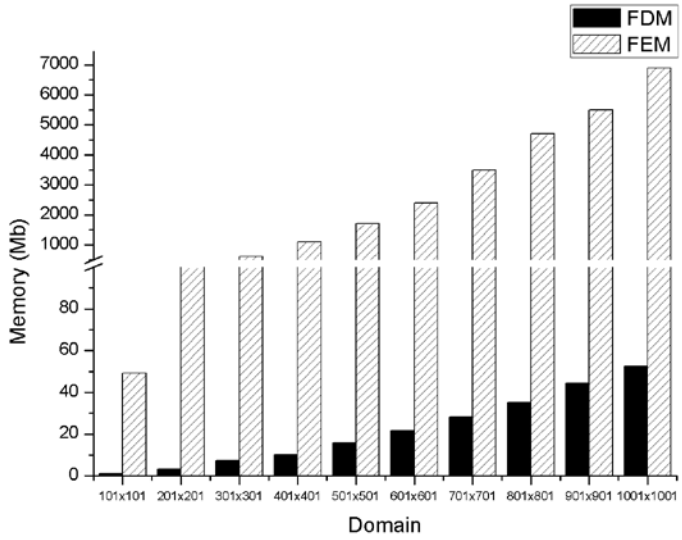

(a)

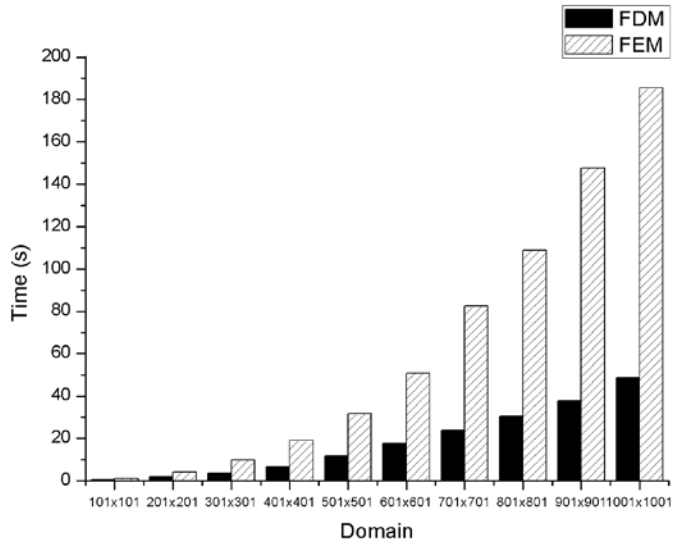

(b)

Figure 2. Required (a) memory and (b) time to perform wave propagation modeling in the time domain using FDM and the Laplace-Fourier domain using FEM.

3.2 Synthetic data FWI Example

3.2.1 Model 94 synthetic onshore data

We applied the proposed algorithm to the Model 94 synthetic model (Gray and Marfurt, 1995), which is based on the complex geometry of the Canadian Foothills. We modified the size of the P-wave velocity model and generated the S-wave velocity model by assuming the Poisson's ratio as 0.25. The density was generated from Gardner's relation (Gardner et al., 1974). The number of shots was 301 and the shot spacing was 50 m. Each shot had 601 receivers, which were separated by 25 m. The receivers recorded signals for 8 s and recording interval was 4 ms. The velocity and density models were 15.025 km wide by 7.525 km deep. The true P-wave, S-wave velocity and density models are shown in Figure 3. Synthetic shot gathers were computed with staggered-grid finite-difference method which is the same algorithm used for forward modeling and backward modeling in the inversion process. Source wavelet that we used to generate synthetic shot gathers was ricker wavelet with 20 Hz of maximum frequency.

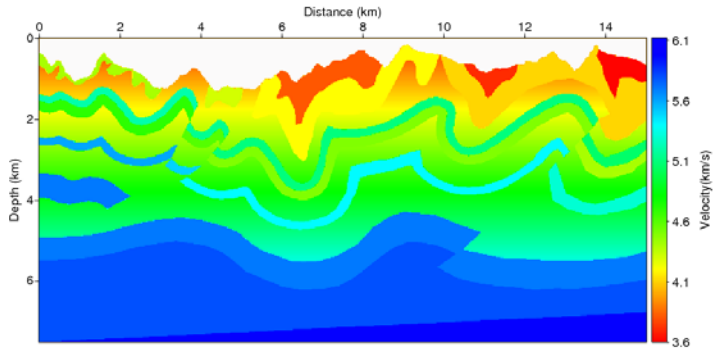

(a)

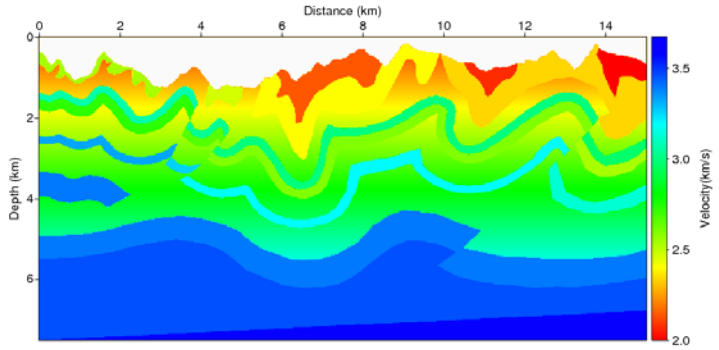

(b)

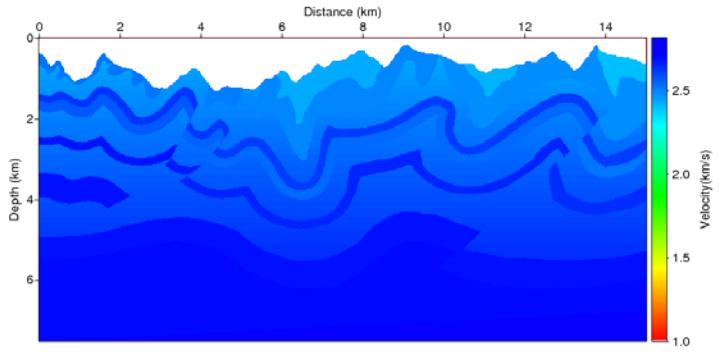

(c)

Figure 3. Model 94 synthetic model of (a) P-wave velocity, (b) S-wave velocity and (c) Density

3.2.2 Laplace-Fourier domain FWI

For Laplace-Fourier-domain FWI, we used 6 different complex frequency ($s = \sigma + \omega$) groups sequentially. The complex frequencies and the number of iterations for each group are given in Table 3. We used 301 shots with interval of 50 m and 601 receivers per shot with interval of 25 m for the FWI. The estimated source wavelet was used for FWI (Shin and Min, 2006). The initial models are shown in Figure 4. We used models that increase linearly with the depth for the P-wave velocity, S-wave velocity and density.

Figure 5 shows the inverted long wavelength velocity models obtained after 240 iterations of the Laplace-Fourier domain FWI. At the shallow part of the inverted P-wave velocity and S-wave velocity, structures are similar to the true velocity models. The overall trend of inverted velocities follows the true velocity models with long wavelength structures. The inverted density is not as good as inverted P-wave and S-wave velocities. These models can be used as the initial velocity models for frequency domain FWI to obtain high-resolution images. To verify the FWI results, we first compared Laplace-Fourier-transformed wavefields. Figure 6 presents the Laplace-Fourier-transformed wavefields of the 150^{th} shot gather obtained after 240 iterations. As we calculated the residual in the Laplace-Fourier domain, the wavefield fitness in the Laplace-Fourier domain is important. The results show that the recorded wavefield and modeled wavefield transformed respect to the each complex frequency are well fitted. Even thought, the amplitude information is more important than the phase information for the Laplace-Fourier domain FWI, we cannot ignore the phase information. To compare the amplitude and phase of the wavefield together, we extracted time traces from 0.4 second to 2.0 second at the 150^{th} shot gather made from the true model, initial model

and inverted model, respectively. Comparison of the time traces is plotted in Figure 7. The amplitude and phase of the time trace from the initial models are not similar to those of the time trace from true models. However, the time trace extracted from the inverted models fits well with the trace from the true models. These results mean that the Laplace-Fourier domain FWI successfully inverted the long wavelength models. To obtain the high-resolution images, we performed frequency domain FWI with a low damping constant. We employed the models in Figure 5 as the initial models. The complex frequency ($s = \sigma + i\omega$) groups used are given in Table 4. Figure 8 shows the inverted images after 187 frequency domain FWI iterations. Figure 8(a) is the inverted P-wave velocity. It inverted most of the structures in the true P-wave velocity model with high-resolution and correct values. Figure 8 (b) is the inverted S-wave velocity. The structures upper the 4-km-deep are well inverted. However, deeper than 4 km, we cannot figure out the exact structures. Figure 8 (c) is the inverted density. We can see the clear lines located on the exact location, but the values are not correctly inverted. Figure 9, Figure 10 and Figure 11 present the P-wave velocity vertical profiles, S-wave velocity vertical profiles and density vertical profiles at 1.875 km and 8.75 km from the left edge, respectively. The vertical profiles of the Laplace-Fourier domain FWI results represent the same overall trends as the vertical profiles of true models. These results demonstrate that the use of proposed algorithm is acceptable because the purpose of the Laplace-Fourier FWI is to invert the long wavelength model. The profiles of the frequency domain FWI results are in good agreement with the profiles of true models.

No.	ω (Hz)	σ (1/s)	Iterations
1	$2\pi \times 0.1$	3, 5, 7, 9	60
2	$2\pi \times 0.3$	3, 5, 7, 9	35
3	$2\pi \times 0.8$	3, 5, 7, 9	34
4	$2\pi \times 1.2$	3, 5, 7, 9	24
5	$2\pi \times 2.0$	3, 5, 7, 9	47
6	$2\pi \times 2.4$	3, 5, 7, 9	40

Table 3. Complex frequency groups for the Laplace-Fourier domain FWI used to invert Model 94 synthetic data

No.	ω (Hz)	σ (1/s)	Iterations
1	$2\pi \times (2.5, 3.0, 3.75, 5.3)$	0.5	40
2	$2\pi \times (5.3, 5.6, 6.2, 6.8, 7.5)$	0.5	40
3	$2\pi \times (7.8, 8.7, 9.6, 10.5)$	1	40
4	$2\pi \times (11.25, 13.2, 15.6)$	1	40
5	$2\pi \times (17.5, 19.5)$	1	27

Table 4. Complex frequency groups for the frequency domain FWI used to invert Model 94 synthetic data

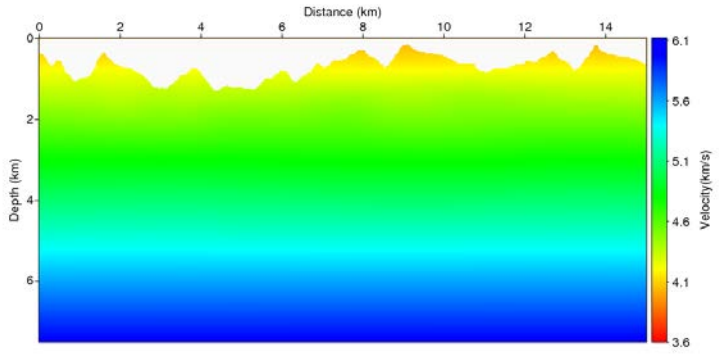

(a)

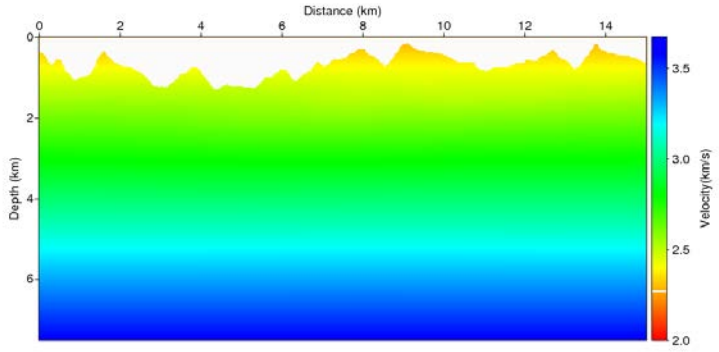

(b)

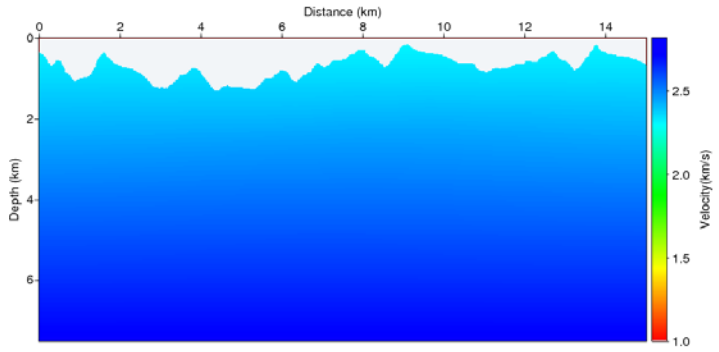

(c)

Figure 4. Initial model of (a) P-wave velocity, (b) S-wave velocity and (c) Density for the Laplace-Fourier domain FWI

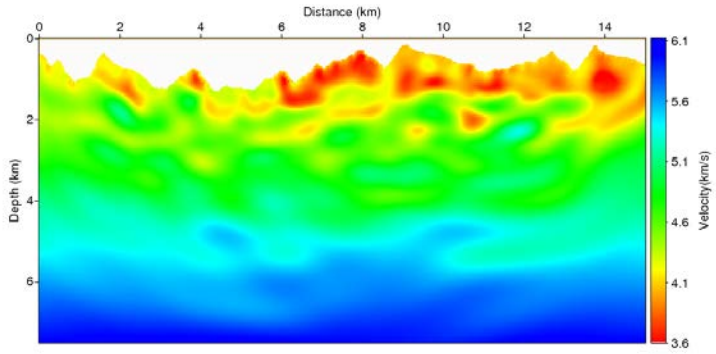

(a)

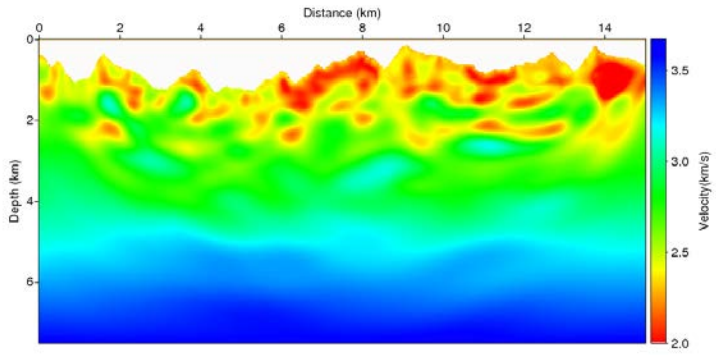

(b)

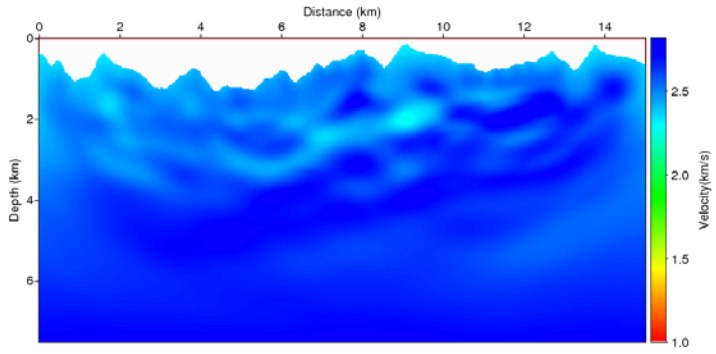

(c)

Figure 5. Inverted model of (a) P-wave velocity, (b) S-wave velocity and (c) Density of the Laplace-Fourier domain FWI at the 240th iteration.

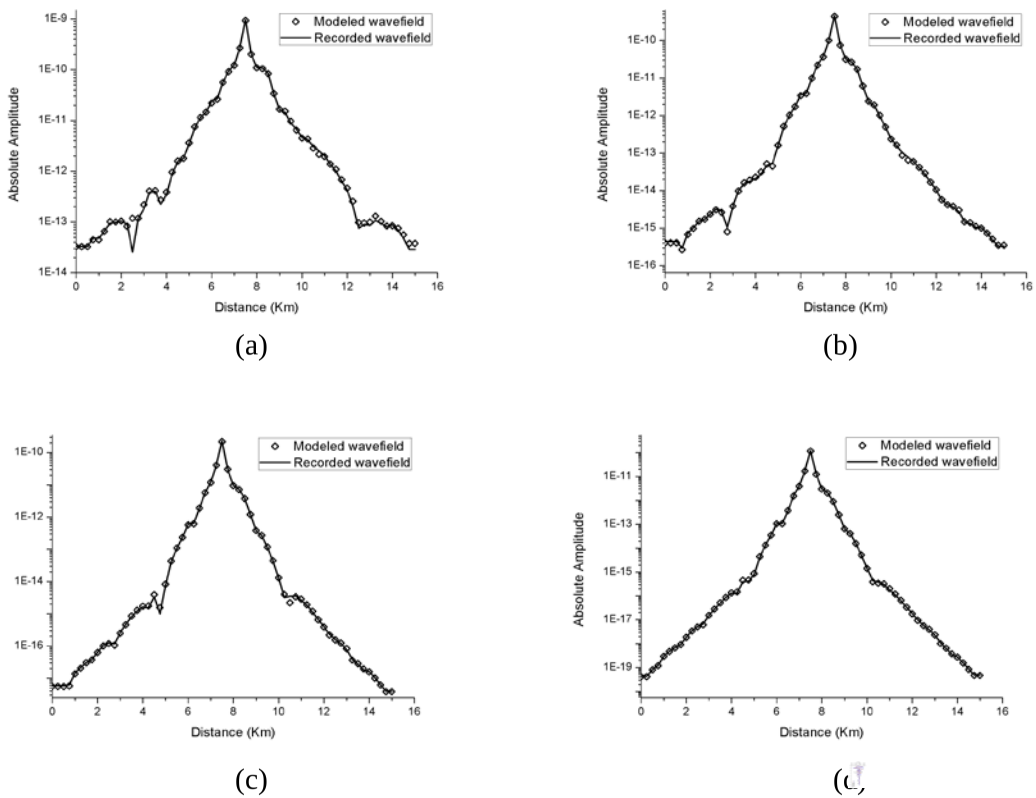

Figure 6. Laplace-Fourier-transformed wavefield where $\omega = 2\pi \times 2.4$ (Hz) and (a) $\sigma = 3$ (1/s), (b) $\sigma = 5$ (1/s), (c) $\sigma = 7$ (1/s) and (d) $\sigma = 9$ (1/s)

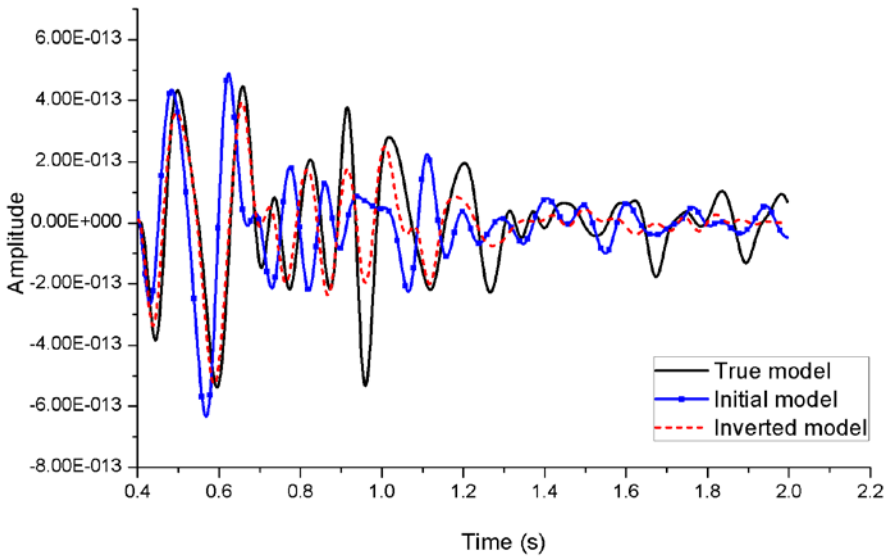

Figure 7. Time traces from 0.4 s to 2.0 s at 150th shot gather generated from true models, initial models and the Laplace-Fourier domain FWI inverted models

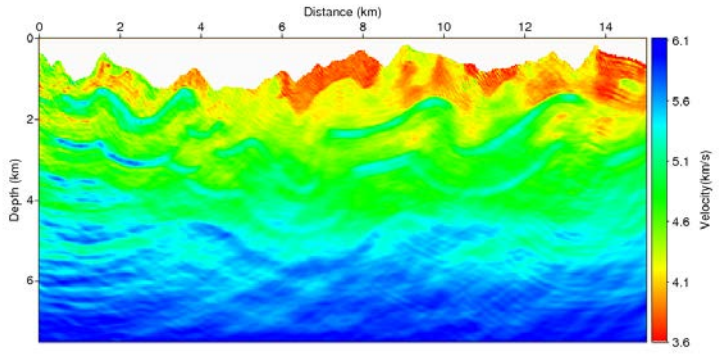

(a)

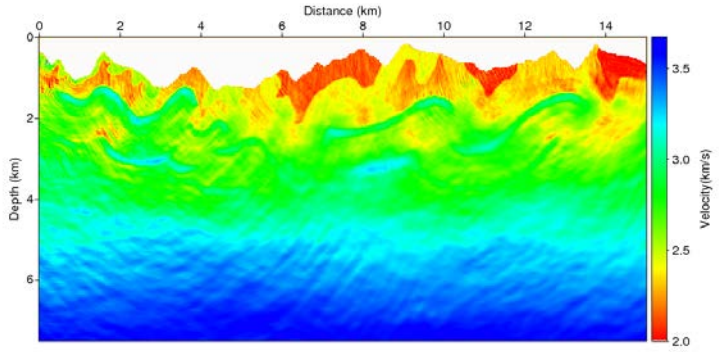

(b)

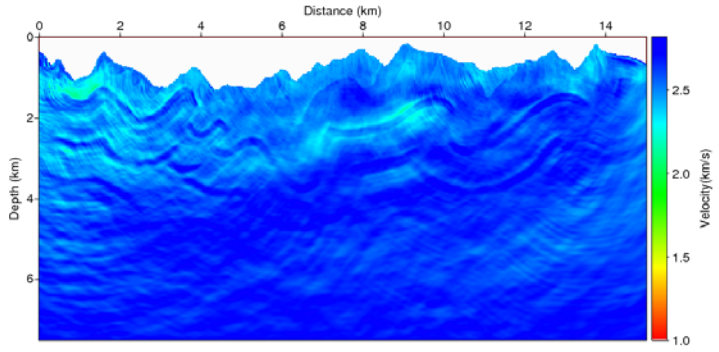

(c)

Figure 8. Inverted model of (a) P-wave velocity, (b) S-wave velocity and (c) Density of the frequency domain FWI at the 187th iteration.

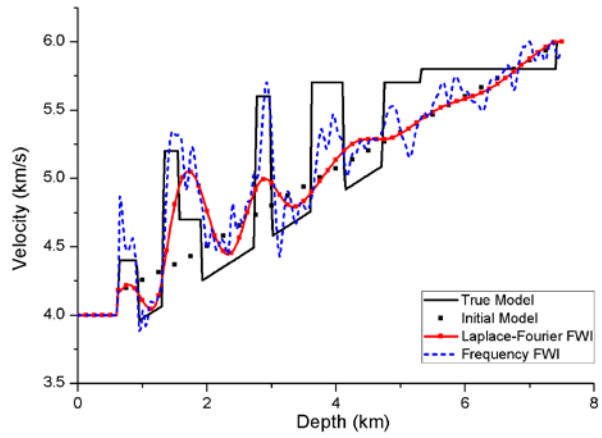

(a)

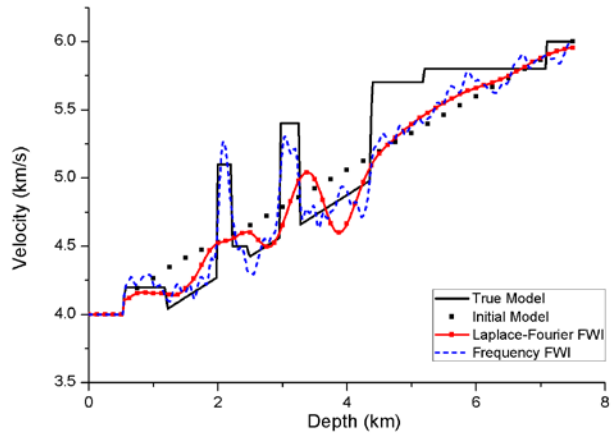

(b)

Figure 9. Vertical profiles of P-wave velocity at (a) 1.875 km and (b) 8.75 km from the left edge.

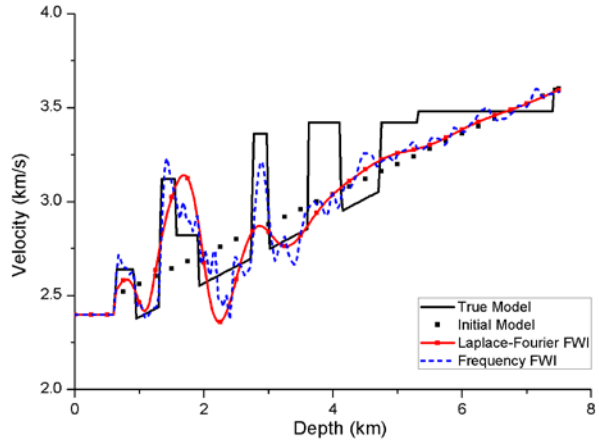

(a)

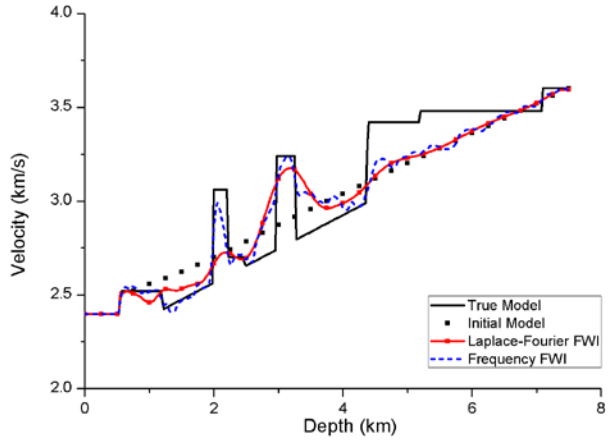

(b)

Figure 10. Vertical profiles of S-wave velocity at (a) 1.875 km and (b) 8.75 km from the left edge

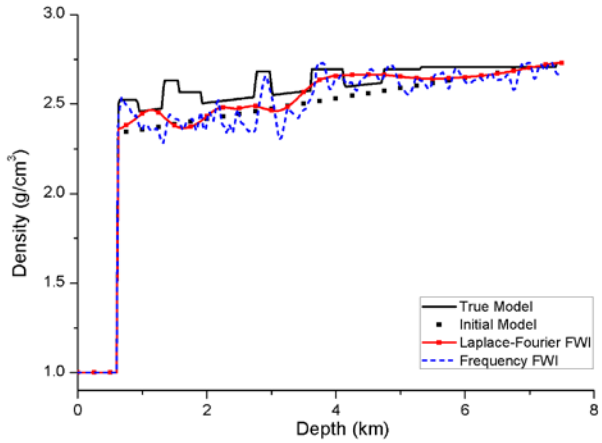

(a)

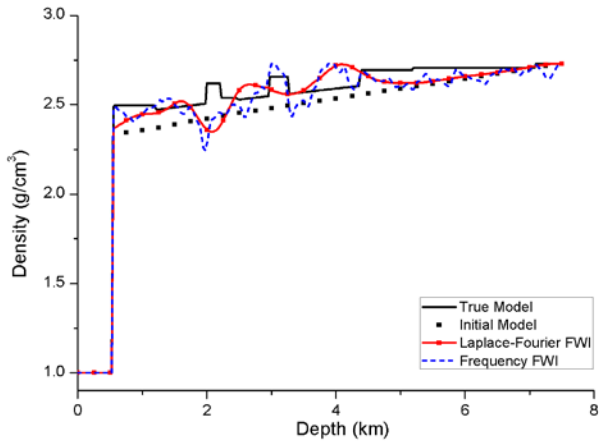

(b)

Figure 11. Vertical profiles of Density at (a) 1.875 km and (b) 8.75 km from the left edge

3.3 Field data FWI Example

3.3.1 Benjamin Creek field onshore data

The Benjamin Creek data set was provided by the CSEG (Canadian Society of Exploration Geophysicists) Workshops on Structural Imaging in the mid-1990s. The data was recorded from Alberta, Canada. It has Canadian foothill geometry. This data set has 143 shots with a shot spacing of 100 m, and approximately 300 receivers per shot. The receiver spacing is 20 m, and the terrain elevation changes as much as 300 m along the line. The velocities and density models are 14.5 km wide by 7.0 km deep. The original shot gathers are in Figure 12.

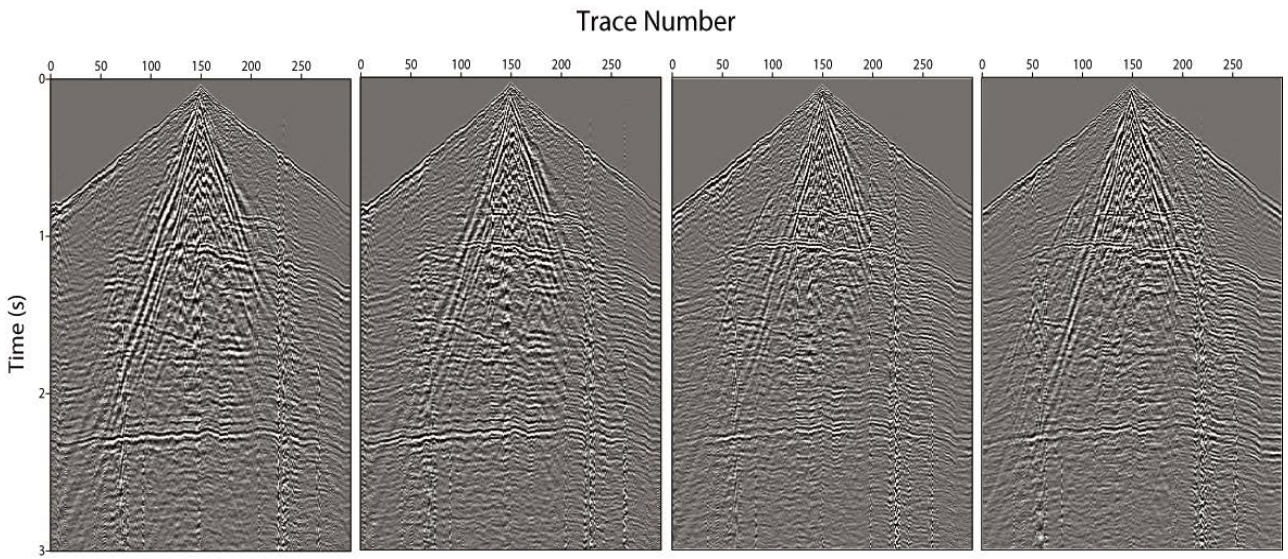

Figure 12. The (a) 88th, (b) 89th, (c) 90th and (d) 91th shot gather of the Benjamin Creek data set

3.3.2 Laplace-Fourier domain FWI

For the Laplace-Fourier FWI, we used 5 different complex frequency groups. The complex frequencies and number of iterations for each group are listed in Table 5. The estimated source wavelet was used for the FWI. Before the FWI, we performed signal muting before the first arrival because the signals emerge earlier than the first arrival can be severe noise in the Laplace-Fourier domain FWI. Also we eliminated bad traces. The initial models of P-wave and S-wave velocities increased linearly with the depth, and a homogeneous density model was employed as shown in Figure 13 (a), (b) and (c), respectively.

Figure 14 shows the inverted long wavelength models for the P-wave velocity, S-wave velocity and density after 117 iterations of the Laplace-Fourier domain FWI. In the real seismic data, the signals are attenuated by subsurface materials in three dimensions during propagating in the heterogeneous Earth (Fichtner et al., 2008). The Laplace-Fourier domain FWI uses the Laplace damping constant, allowing it to capture the three dimensional attenuation with the two dimensional FWI algorithm. However, it is difficult to model the three dimensional attenuation with the two dimensional frequency domain FWI algorithm. Therefore, we did not perform frequency domain FWI.

To validate the Laplace-Fourier domain FWI results, we performed RTM using the P-wave velocity. Figure 15 shows the RTM results using the initial and inverted P-wave velocity. The RTM result obtained with the inverted velocity gives a more detailed image of subsurface structures with a higher concentration of lines than the result obtained with the initial velocity. For a more detailed comparison, we first compared the reference prestack depth

migration result from Wu et al. (1998) (Figure 16) with the RTM results from the initial and inverted P-wave velocity. There are three major reflectors located on about 3 km depth, 5 km depth and 7 km depth. When the accurate velocity is used as a background velocity for RTM, the reflectors would be located on the exact location. The reflectors in RTM result from inverted velocity located on the same position as the reference result. However, the reflectors in RTM result from initial velocity are not in the exact locations. The first reflector is located on 2 km depth, the second reflector is located in 4 km depth and the third reflector is located on 5 km depth. These results mean that the Laplace-Fourier domain FWI inverted velocity correctly. We also compared the common image gathers (CIGs). We extracted CIGs from three different locations: 2 km, 7 km and 10 km from the left edge of the model. Most of the reflectors in Figure 18 are flatter than those in Figure 17. In the Figure 18(a), most of the reflectors are flat but the reflectors in Figure 17(a) are not at enough. The reflectors at 2 km, 3 km and 5 km depth in Figure 17(b) are curved and not concentrated enough while the reflectors at the same location in Figure 18(b) show better flatness and concentration. If we compare the base rock in Figure 17(c) and Figure 18(c), we can find out that the base rock in Figure 18(c) is well located about 6 km depth with better flatness. In addition, we compared Laplace-Fourier-transformed wavefield of recorded data and modeled data. In Figure 19, we plotted Laplace-Fourier-transformed wavefields of the 60^{th} shot gather at the last iteration of the FWI. The waveforms of recorded data are severely fluctuating because the data is real onshore data with foothill geometry. Even though the severe fluctuation, we can figure out that the transformed wavefields of the modeled data are well fitted with the transformed wavefields of the recorded data. These results show that the velocity was successfully inverted by the Laplace-Fourier

domain FWI.

No.	ω (Hz)	σ (1/s)	Iterations
1	$2\pi \times 0.3$	1, 3, 5	13
2	$2\pi \times 1.2$	1, 3, 5	21
3	$2\pi \times 2.4$	1, 3, 5	23
4	$2\pi \times 3.6$	1, 3, 5	30
5	$2\pi \times 5.5$	1, 3, 5	30

Table 5. Complex frequency groups for the Laplace-Fourier domain FWI used to invert Benjamin Creek field data.

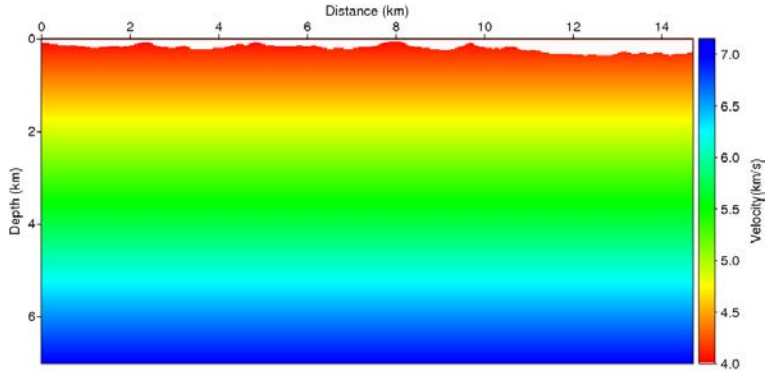

(a)

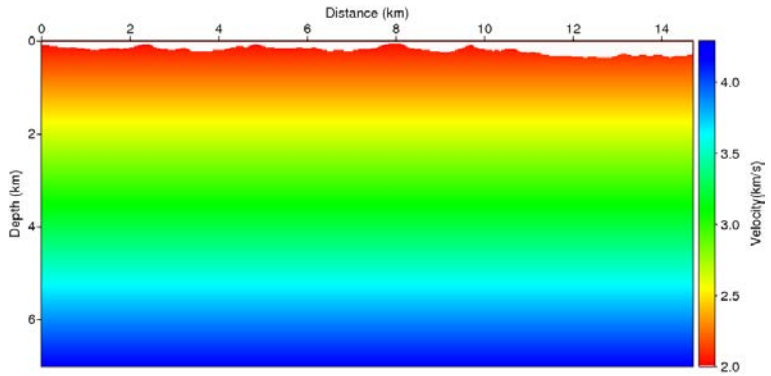

(b)

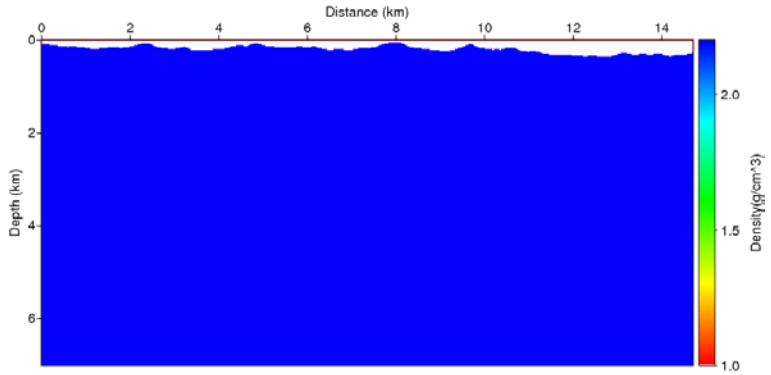

(c)

Figure 13. Initial model of (a) P-wave velocity, (b) S-wave velocity and (c) Density for the Laplace-Fourier domain FWI

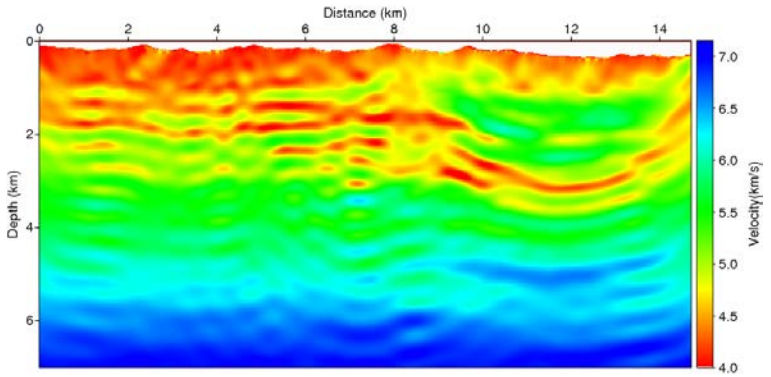

(a)

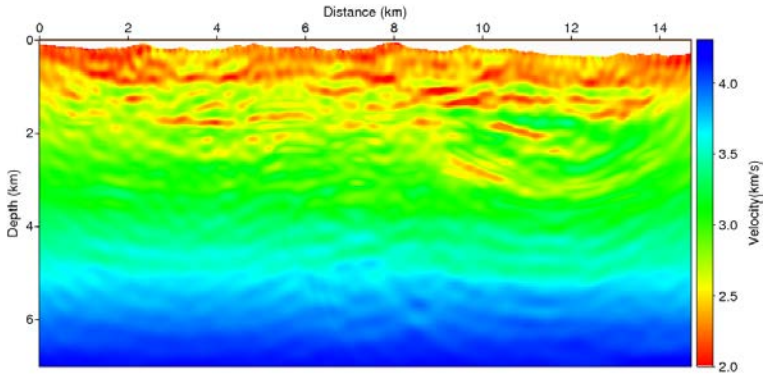

(b)

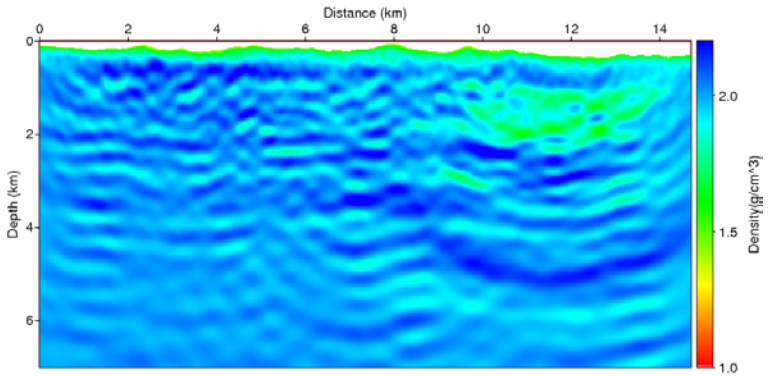

(c)

Figure 14. Inverted model of (a) P-wave velocity, (b) S-wave velocity and (c) Density of the Laplace-Fourier domain FWI at the 117th iteration.

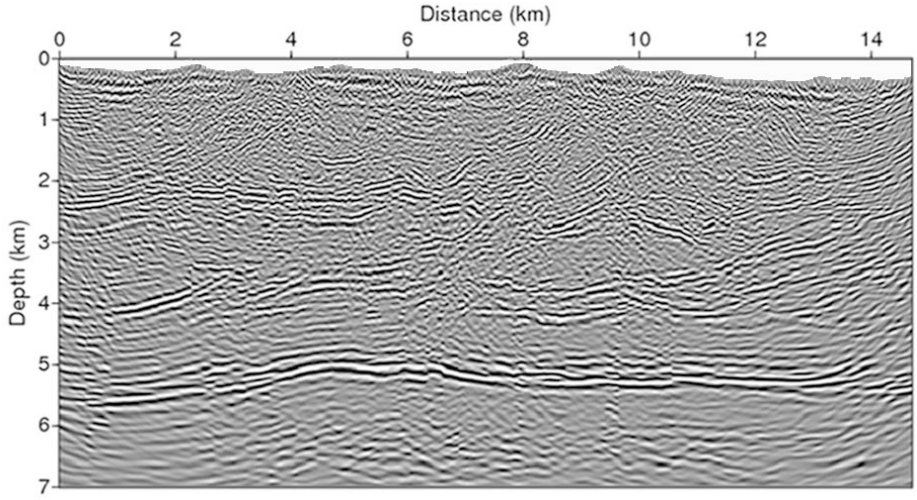

(a)

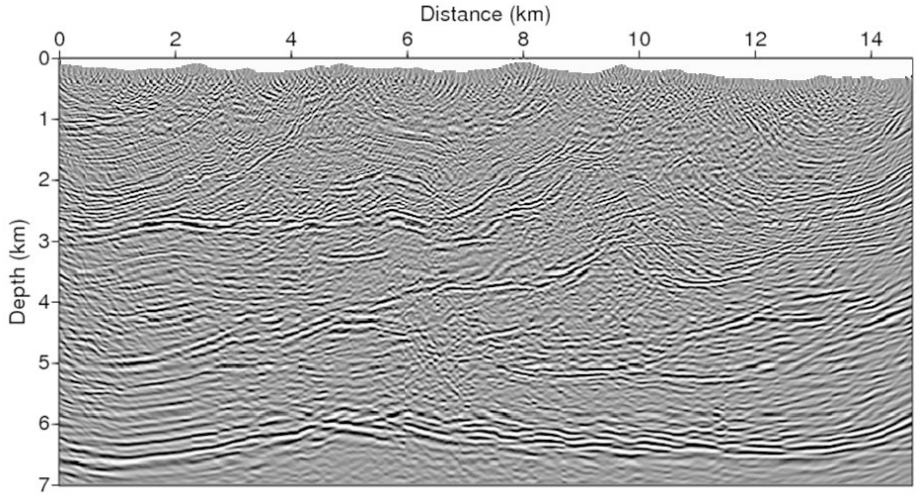

(b)

Figure 15. RTM result obtained from (a) the initial P-wave velocity and (b) the inverted P-wave velocity

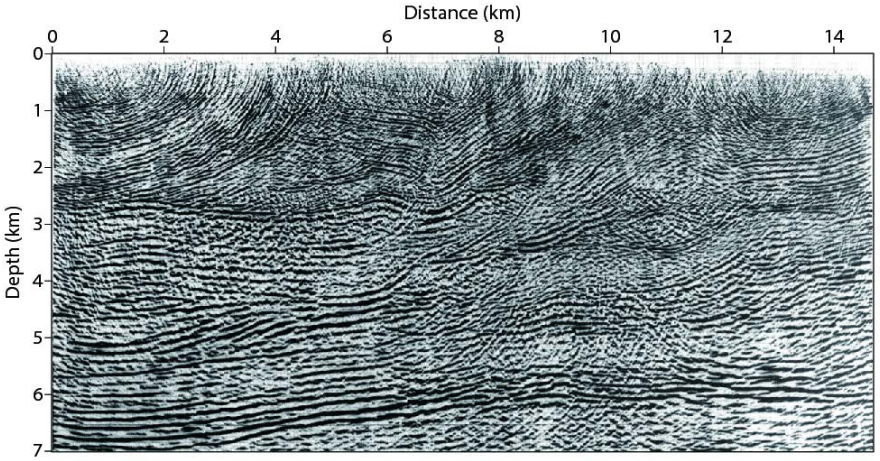

Figure 16. Prestack depth migration result from Wu et al. (1998)

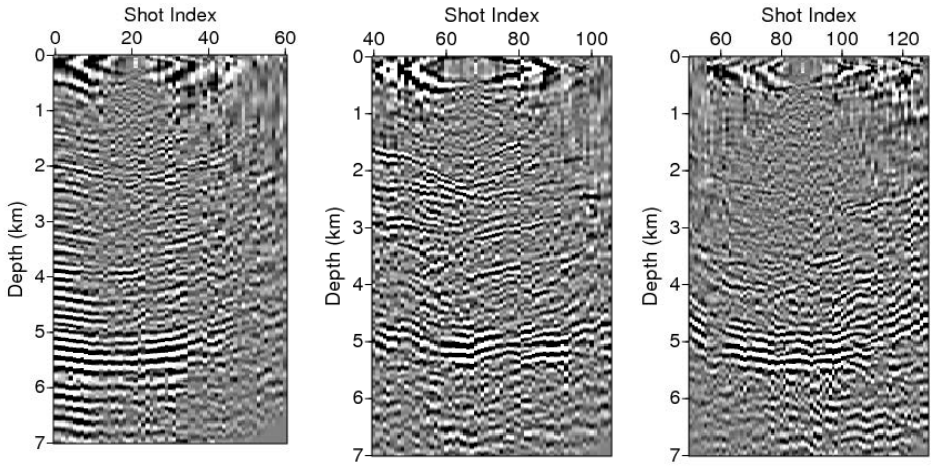

(a) (b) (c)

Figure 17. Common Image Gathers at (a) 2 km, (b) 7 km and (c) 10 km from the left edge of the model when the initial velocity is used as the background velocity of RTM.

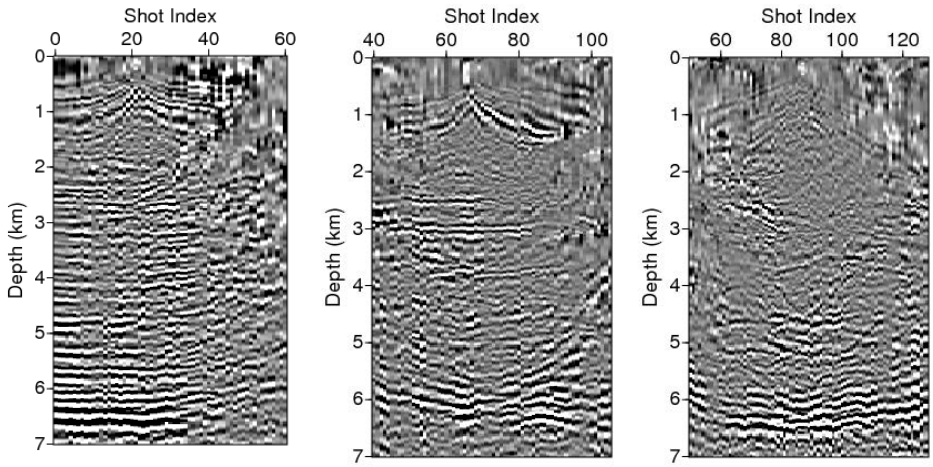

(a) (b) (c)

Figure 18. Common Image Gathers at (a) 2 km, (b) 7 km and (c) 10 km from the left edge of the model when the inverted velocity is used as the background velocity of RTM.

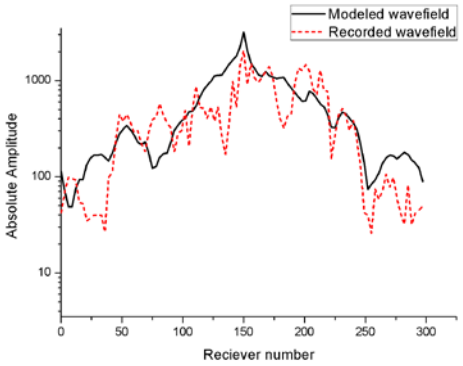

(a)

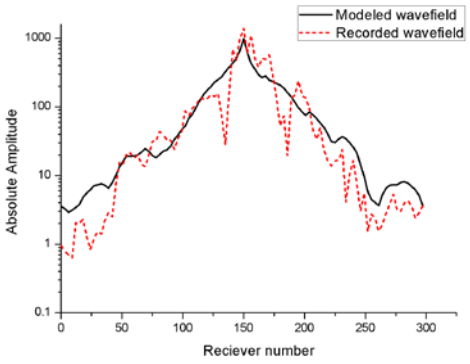

(b)

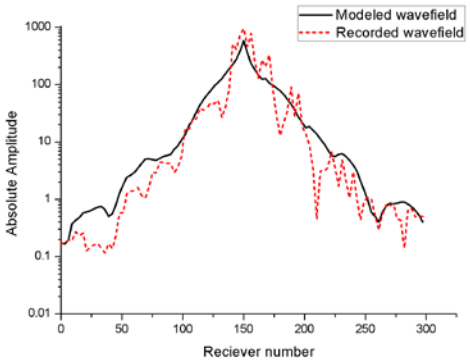

(c)

Figure 19. Laplace-Fourier-transformed wavefield where $\omega = 2\pi \times 5.5$ (Hz) and (a) $\sigma = 1\ (1/s)$, (b) $\sigma = 13(1/s)$ and (c) $\sigma = 5\ (1/s)$

Chapter 4 Conclusions

We developed Laplace-Fourier domain elastic FWI using time domain wave propagation modeling algorithm to invert the P-wave velocity, S-wave velocity and density from elastic seismic data. We applied our new algorithm to elastic onshore data. First, Model 94 synthetic onshore data was inverted using the proposed FWI algorithm. After inverting the long wavelength models, we conducted frequency domain FWI to obtain high-resolution images. The Laplace-Fourier-transformed wavefields of the modeled and recorded data were compared. The wavefields of the modeled data were in good agreement with those of the recorded data. To compare the phase and amplitude of the seismogram simultaneously, we obtained time traces from three different seismograms by using true models, initial models and inverted models. Time trace from inverted models shows good correlation with the trace from true models. The vertical profiles of the P-wave and S-wave velocities and density also show the long wavelength models were successfully inverted from the Laplace-Fourier domain FWI. These results show that the proposed FWI algorithm successfully inverted the long wavelength models. Next, our algorithm was applied to Benjamin Creek field onshore data. The RTM results obtained with the initial and inverted P-wave velocities as the background velocity model were compared to validate our algorithm. The lines in the migration image obtained from the inverted velocity model were better resolved than those obtained from the initial velocity model. Specifically, three major reflectors were compared with the reflectors in reference depth migration image. We also compared CIGs of each migration result. Most of the reflectors in the CIGs based on the inverted

velocity model were flatter and more concentrated than those in the CIGs based on the initial velocity model. Finally, we compared Laplace-Fourier-transformed wavefields of the modeled and recorded data. The results show that the wavefields fit well each other. However, we did not apply frequency domain FWI to the real onshore data because it is hard to model the three dimensional wave attenuation with the two dimensional FWI algorithm. Through this study multi-parameters were successfully inverted with the proposed algorithm. However, the proposed algorithm still has some limits. First, while P-wave velocity and S-wave velocity were inverted to the right direction, density is not well inverted. Second, complex frequencies are selected based on the trial and error. Therefore, we need to improve the algorithm to invert density correctly. Proper way to select the complex frequency groups should also be studied. Moreover, the future work would involve the extension of our algorithm to three-dimensional elastic FWI.

Chapter 5 References

Bae, H., C. Shin, Y. Cha, Y. Choi, and D. Min, 2010, 2d acoustic-elastic coupled waveform inversion in the laplace domain: Geophysical Prospecting, 58, 997-1010.

Ben-Hadj-Ali, H., S. Operto, and J. Virieux, 2008, Velocity model building by 3d frequency-domain, full-waveform inversion of wide-aperture seismic data: Geophysics, 73, VE101-VE117.

Brenders, A. J., and R. G. Pratt, 2007, Full waveform tomography for lithospheric imaging: results from a blind test in a realistic crustal model: Geophysical Journal International, 168, 133-151.

Brossier, R., S. Operto, and J. Virieux, 2009, Seismic imaging of complex onshore structures by 2d elastic frequency-domain full-waveform inversion: Geophysics, 74, WCC105-WCC118.

Bunks, C., F. M. Saleck, S. Zaleski, and G. Chavent, 1995, Multiscale seismic waveform inversion: Geophysics, 60, 1457-1473.

Cerjan, C., D. Koslo, R. Koslo, and M. Reshef, 1985, A nonreecting boundary condition for discrete acoustic and elastic wave equations: Geophysics, 50, 705-708.

Choi, Y., D. Min, and C. Shin, 2008, Two-dimensional waveform inversion of multicomponent data in acoustic-elastic coupled media: Geophysical Prospecting, 56, 863-881.

Chung, W., C. Shin, and S. Pyun, 2010, 2d elastic waveform inversion in the

laplace domain: Bulletin of the Seismological Society of America, 100, 3239-3249.

Claerbout, J. F., 1971, Toward a unied theory of reector mapping: Geophysics, 36, 467-481.

Crase, E., A. Pica, M. Noble, J. McDonald, and A. Tarantola, 1990, Robust elastic nonlinear waveform inversion: application to real data: Geophysics, 55, 527-538.

Davis, T., 2006, Umfpack version 5: University of Florida.

Fichtner, A., B. L. N. Kennett, H. Igel, and H. P. Bunge, 2009, Full seismic waveform tomography for upper-mantle structure in the australasian region using adjoint methods:Geophysical Journal International, 179, 1703-1725.

Fichtner, A., J. Trampert, P. Cupillard, E. Saygin, T. Taymaz, Y. Capdeville, and A. Villaseor, 2013, Multiscale full waveform inversion: Geophysical Journal International,194, 534-556.

Gardner, G. H. F., L. W. Gardner, and A. R. Gregory, 1974, Formation velocity and density - the diagnostic basics for stratigraphic traps: Geophysics, 39, 770-780.

Gauthier, O., J. Virieux, and A. Tarantola, 1986, Two-dimensional nonlinear inversion of seismic waveforms: Numerical results: Geophysics, 51, 1387-1403.

Graves, R. W., 1996, Simulating seismic wave propagation in 3d elastic media using staggered-grid finite difference: Bull. Seism. Soc. Am., 86, 1091-1106.

Gray, S. H., and K. J. Marfurt, 1995, Migration from topography: Improve the

near-surface image: Canadian Journal of Exploration Geophysics, 31, 18-24.

Guitton, A., and W. W. Symes, 2003, Robust inversion of seismic data using the huber norm: Geophysics, 68, 1310-1319.

Ha, T., W. Chung, and C. Shin, 2009, Waveform inversion using a back-propagation algorithm and a huber function norm: Geophysics, 74, R15-R24.

Ha, W., S. Pyun, J. Yoo, and C. Shin, 2010, Acoustic full waveform inversion of synthetic land and marine data in the laplace domain: Geophysical Prospecting, 58, 1033-1047.

Huber, P. J., 1973, Robust regression: Asymptotics, conjectures, and monte carlo: Ann. Statist., 1, 799-821.

Igel, H., H. Djikpss, and A. Tarantola, 1996, Waveform inversion of marine reection seismograms for p impedance and poisson's ratio: Geophysical Journal International, 124, 363-371.

Kim, J. H., and S. J. kim, 1999, A multifrontal solver combined with grahp partitioner: AIAA Journal, 37, 964-970.

Kim, Y., C. Shin, and H. Calandra, 2013, An algorithm for 3d acoustic time-laplace-fourier domain hybrid full waveform inversion: Geophysics, 78, R151-R161.

Lailly, P., 1983, The seismic inverse problem as a sequency of before stack migrations: Society for Industrial and Applied Mathematics, Expanded Abstracts, 206-220.

Levander, R. A., 1988, Fourth-order nite-dierence p-sv seismograms: Geophysics, 53, 1425-1436.

Madariaga, R., 1976, Dynamics of an expanding circular fault: Seism. Soc. Am., 66, 163-182.

Marquardt, D. W., 1963, An algorithm for least squares estimation of non-linear parameters:Journal of the Society of Industrial and Applied Mathematics, 11, 431-441.

Mora, P. R., 1987, Ninlinear two-dimensional ealstic inversion of multioset seismic data:Geophysics, 52, 1211-1228.

Operto, S., C. Ravaut, L. Improta, J. Virieux, A. Herrero, and P. Dell'Aversana, 2004, Quantitative imaging of complex structures from dense wide-aperture seismic data by multiscale traveltime and waveform inversions: a case study: Geophysical Prospecting, 52, 625-651.

Operto, S., J. Virieux, P. Amestoy, J. L'Excellent, L. Giraud, and H. Ben-Hadj-Ali, 2007, A multifrontal solver combined with grahp partitioner: Geophysics, 72, SM195-SM211.

Plessix, R. E., 2009, Three-dimensional frequency-domain full-waveform inversion with an iterative solver: Geophysics, 74, WCC149-WCC157.

Pratt, R. G., C. Shin, and G. J. Hicks, 1998, Gauss-newton and full newton methods in frequency-space seismic waveform inversion: Geophysical Journal international, 133, 341-362.

Pyun, S., W. Son, and C. Shin, 2011, 3d acoustic waveform inversion in the laplace domain using an iterative solver: Geophysical Prospecting, 59, 386-399.

Ravaut, C., S. Operto, L. Improta, J. Virieux, A. Herrero, and P. Dell'Aversana, 2004, Multiscale imaging of complex structures from multifold wideaperture

seismic data by frequencydomain fullwaveform tomography: application to a thrust belt: Geophysical Journal International, 159, 1032-1056.

Romdhane, A., G. Grandjean, R. Brossier, F. Rejiba, S. Operto, and J. Virieux, 2011, Shallow-structure characterization by 2d elastic full-waveform inversion: Geophysics, 76, R81-R93.

Sears, T. J., S. C. Singh, and P. J. Barton, 2008, Elastic full waveform inversion of multicomponent obc seismic data: Geophysical Prospecting, 56, 843-862.

Sheng, J., A. Leeds, M. Buddensiek, and G. T. Schuster, 2006, Early arrival waveform tomography on near-surface refraction data: Geophysics, 71, U47-U57.

Shin, C., and Y. H. Cha, 2008, Waveform inversion in the laplace domain: Geophysical Journal International, 173, 922-931.

-, 2009, Waveform inversion in the laplace-fourier domain: Geophysical Journal International, 177, 1067-1079.

Shin, C., S. Jang, and D. Min, 2001, Improved amplitude preservation for prestack depth migration by inverse scattering theory: Geophysical Prospecting, 49, 592-606.

Shin, C., and D. Min, 2006, Waveform inversion using a logarithimic waveeld: Geophysics, 71, R31-R42.

Shipp, R. M., and S. C. Singh, 2002, Two-dimensional full waveeld inversion of wide-aperture marine seismic streamer data: Geophysical Journal International, 73, VE101-VE117.

Sirgue, L., J. T. Etgen, and U. Albertin, 2008, 3d frequency domain waveform inversion using time domain nite dierence methods: 70th EAGE Conference and Exhibition Extended Abstracts.

Sirgue, L., and R. G. Pratt, 2004, Ecient waveform inversion and imaging: A strategy for selecting temporal frequencies: Geophysics, 69, 231-248.

Tarantola, A., 1984, Inversion of seismic reection data in the acoustic approximation: Geophysics, 49, 1259-1266.

-, 1986, A strategy for nonlinear elastic inversion of seismic reection data.: Geophysics, 51, 1893-1903.

Trefethen, L. L., and D. Bau, 1997, Numerical linear algebra: SIAM.

Virieux, J., 1986, P-sv wave propagation in heterogeneous media: velocity-stress finite difference method: Geophysics, 51, 889-901.

Whitmore, N. D., 1983, Iterative depth migration by backward time propagation: Society of exploration geophysicists.

Wu, W. J., L. Lines, A. Burton, H. X. Lu, J. Zhu, W. Jamison, and R. P. Bording, 1998, prestack depth migration of an alberta foothills data set-the husky experience: Geophysics, 63, 392-398.

Yan, J., and P. Sava, 2008, Isotropic angle-domain elastic reverse-time migration: Geophysics, 73, S229-S239.

초 록

육상 탄성파 탐사 자료를 통해 음향파 완전 파형 역산을 이용하여 지하 구조에 대한 정보를 얻기 위해서는 그라운드 롤과 모드 변환 파들과 같은 탄성파의 영향을 억제 해야 한다. 많은 전처리를 통해 탄성파의 영향을 억제 하는 과정 중에 음향파에 대한 변형 또한 피할 수 없다. 게다가 실체파와 표면파를 완전히 분리해내는 것은 거의 불가능에 가깝다. 이러한 이유로 실제 파형과 더 유사한 파를 만들어 내기 위해 모델링 단계에서 두 종류의 파를 모두 만들어낼 필요가 있다. 따라서 정확한 완전 파형 역산을 위해서는 탄성파동방정식을 이용한 탄성파 완전 파형 역산이 필수적이다. 또한 탄성파 완전 파형 역산은 P파 속도뿐만 아니라 S파 속도와 밀도 정보도 함께 역산 할 수 있어서 음향파 완전 파형 역산보다 더 많은 지질학적인 정보를 제공해 줄 수 있다. 시간 영역 모델링을 이용한 라플라스-푸리에 영역 완전 파형 역산은 시간 영역 파동 전파 모델링과 라플라스-푸리에 영역 완전 파형 역산을 결합한 알고리즘이다. 정 전파 파동장과 역 전파 파동장을 시간 영역에서 얻기 위하여 엇격자 유한 차분법이 사용되었다. 탐사 자료와 모델링 자료간의 잔차, 가상 송신원, 헤시안 그리고 구배도는 라플라스-푸리에 영역에서 계산 되었다. 우리는 시간 영역 파동 전파 모델링으로 정 전파 및 역 전파 파동장을 구하였는데 이는 시간 영역의 파동장을 라플라스-푸리에 영역 파동장에 비해 더 직관적으로 다룰 수 있어서일 뿐 아니라 행렬 솔버를 이용하지 않고 효율적인 모델링을 할 수 있어서 이다. 최적화 과정은

라플라스-푸리에 영역에서 진행되었는데 왜냐하면 라플라스-푸리에 영역 완전 파형 역산은 저주파 성분이 부족한 실제 현장 자료에 적용이 가능하기 때문이다. 이 연구를 통해 제안된 알고리즘을 검증하기 위해서 인공 합성자료와 실제 탐사 자료에 대해 수치 실험을 진행하였다. 인공 합성자료로는 모델 94 육상 자료를 사용하였고 실제 자료로는 벤자민 크릭 육상 탐사 자료를 사용 하였다.

주요어 : 라플라스-푸리에 영역 완전 파형 역산, 탄성파 완전 파형 역산, 언덕 지형, 육상 탐사 자료

학번 : 2012-21009